Identification of an equivalent viscous damping function depending on engineering demand parameters

T. Heitz, Cédric Giry, B. Richard, F. Ragueneau

HAL Id: hal-02079797
https://hal.science/hal-02079797

Submitted on 22 Oct 2021

Identification of an equivalent viscous damping function depending on engineering demand parameters

T. Heitz[a,*], C. Giry[a,**], B. Richard[b], F. Ragueneau[a]

[a]LMT, ENS Paris-Saclay, CNRS, Université Paris-Saclay. 61, Avenue du Président Wilson, F-94235, Cachan, France
[b]IRSN, 31 avenue du General Leclerc, F-92260, Fontenay aux Roses, France

Abstract

When performing a nonlinear time-history analysis of a reinforced concrete structure, it is necessary for the used structural model to dissipate the correct amount of energy. For the sake of computational efficiency, viscous damping models are still commonly used to account, partially or not, for non-viscous dissipations (e.g. friction between the crack surfaces, bond slip at the steel-concrete interface). In order to improve the physical relevance of such a substitution, an evolving equivalent viscous damping ratio estimated for a simply supported reinforced concrete beam is proposed in this paper. This work takes place in the scope of a moderate seismicity context for which steel yielding is not expected. The results are not directly identified from experimental results but rather from numerical simulations carried out thanks to an equivalent single-degree-of-freedom model, itself calibrated by means of quasi-static experiments. To begin with, the experimental setup used to calibrate the single-degree-of-freedom model and the equivalent viscous damping ratio assessment method are presented. Then, the single-degree-of-freedom model and the identification procedure are exposed. The resulting outputs are presented and commented. Finally, numerical experiments are performed in order to obtain equivalent viscous damping ratio values corresponding to a given maximum time-history curvature and a curvature demand.

Keywords: Dissipations, Reinforced concrete, Viscous damping, Experiments, Model identification

1. Introduction

Despite the increasing accuracy of the models dedicated to the nonlinear behavior of reinforced concrete (RC) structures, their combination with complex finite element (FE) meshes still leads to high computational cost. In practice, an additional viscous damping is often used to account for dissipations not taken into account by the structural model (e.g. [40, 9, 5, 8]). However, it is important to keep in mind that civil engineering structures often do not show purely viscous damping. Some authors [15] state that cracks within damaged elements dissipate a significant amount of energy and this dissipation is better described by a Coulomb friction model rather than a linear viscous one, due to the bond slipping between steel and concrete. This paper focuses on the case of earthquakes that do not induce steel yielding in structures (generally, weak to moderate intensity earthquakes). This choice is based on the French regulatory seismic hazard map [33] in figure 1 where the vast majority of the country presents at most a moderate seismic hazard (scale 3 over 5). In particular, it is considered that the main dissipations occur in the concrete (e.g. crack initiation, propagation and friction). This choice is also supported by the French regulation regarding the design of nuclear power plants where steel yielding is generally considered as non-acceptable. Combining hysteretic and viscous dissipations can compromise the validity of a study [5, 17] and could require a reduction of the viscous damping in the nonlinear range [8]. In order to describe this dependency, several evolving Rayleigh-type viscous damping models have been proposed [25], but experimental evidences on slender buildings tend to show that an adequate modal viscous damping could be an intermediary between constant viscous damping for all modes and stiffness-proportional damping [10, 46]. Before performing such a fine analysis, simplified methodologies should be used in order to obtain a first design of a structure. Alternatively, displacement-based methods[38] have became popular for the past decades, but they generally require the knowledge of a capacity curve and the value of an equivalent viscous damping ratio (EVDR). It is worth mentioning alternative approaches to model nonlinearities, such as the ones relying on the concept of ductility [13, 28]. In this analysis, the damping ratio has a key role when assessing maximum structural responses (i.e. reduction of the demand spectra to represent the nonlinearities of the structure). However, some studies show it is the second source of uncertainties after the ground motions [4, 29], leading so to uncertainty and wrong quantification of the structural response. Furthermore, this assumed equivalence with the energy dissipated hysteretically may be subjected to discussions. Indeed, several studies have emphasized the fact that the viscous damping depends on the response amplitude for RC buildings [31, 32, 46] and on their degradation state often described by a displacement ductility level [45, 16, 21, 26, 37, 12, 44]. In fact, there is actually no reason to keep the EVDR constant

---
*Corresponding author
**Principal corresponding author
Email addresses: thomas.heitz@lmt.ens-cachan.fr (T. Heitz),
cedric.giry@ens-paris-saclay.fr (C. Giry),
benjamin.richard@irsn.fr (B. Richard),
frederic.ragueneau@ens-paris-saclay.fr (F. Ragueneau)

throughout the nonlinear time-history analysis (NLTHA). For instance, [5, 8] have shown that EVDR is not constant in that case due to the continuous change in the modal properties of the structure. To sum-up, the aforementioned papers suggest that the EVDR depends on the degradation state of the structure and on the displacement demand. A correct quantification of energy dissipation according to the degradation state is of main importance for design purposes as well as for the estimation of margin. With a method like the linear equivalent approach, a small change of the EVDR leads to non-negligible differences in the pseudo-acceleration and in the displacement observed by the structure. For instance, according to the formula provided in [7] (1), changing the EVDR from 1% to 2% ($\xi=\xi_0 + \xi_{eq} = 5 + \xi_{eq}$) while considering the nonlinearities leads to a decrease of the design load comprised between 5% and 9%.

$$\eta = \sqrt{\frac{10}{5 + \xi}} \qquad (1)$$

Furthermore, it has been observed and commented that even in the case of a more complex nonlinear computation (see for instance [41, 43]), a small change in the value of the initial viscous damping chosen for the analysis leads to large differences in the response (displacement, floor response spectra,). The RC structural elements show dissipation capacity in their pre-yielding regime. Indeed, nonlinear phenomena also occur in concrete and at its interfaces with steel reinforcements. The quantification of these dissipations is of main concern in the energy production domain. Indeed, the capacity of the structural components to dissipate energy influences directly the loading seen by the sensitive equipments. In the context of accidental loading such as earthquake, one should ensure the functioning of these equipments to maintain the global safety.

The influence of the degradation state of the structure and the displacement demand is investigated in this paper. In the first section, the experimental setup used to calibrate the beam equivalent single-degree-of-freedom (SDOF) model and the EVDR assessment method are presented. Then, the SDOF model formulation and its identification procedure are detailed. Finally, numerical experiments are performed on this model in order to obtain EVDR values corresponding to a maximum relative history displacement and a relative displacement demand.
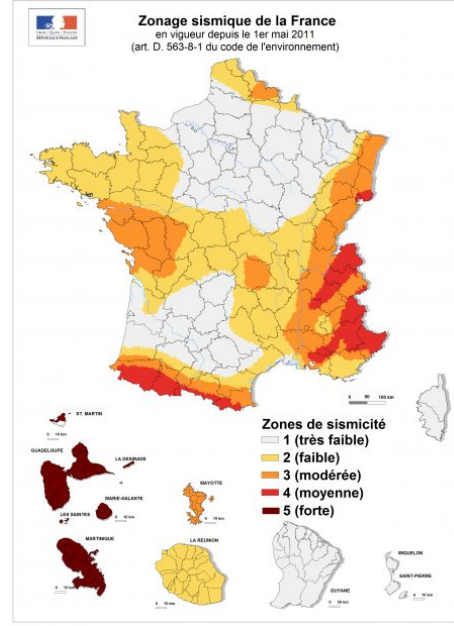

Figure 1: Regulatory seismic hazard map in France (1. very weak [PGA = 0.4 m.s^{-2}], 2. weak [PGA = 0.7 m.s^{-2}], 3. moderate [PGA = 1.1 m.s^{-2}], 4. average [PGA = 1.6 m.s^{-2}], 5. strong [PGA = 3 m.s^{-2}]) [33]

2. Experimental campaign

2.1. Context and motivations

An experimental campaign has been set up on RC beams by means of the AZALÉE shaking table, as part of the TAMARIS experimental facility operated by the French Alternative Energies and Atomic Energy Commission (CEA). The main objective is to provide the scientific and engineering communities reference data through both dynamic and quasistatic tests in order to evaluate the dissipations depending on structural, material and signal characteristics. The measure of damping forces is challenging because their levels are unknown and generally more difficult to investigate than acceleration or restoring forces [24]. Furthermore, they originate from several sources and evolve along the time-history analysis. In order to quantify and to analyze the dissipation and its evolution during quasi-static and dynamic loadings, a dense network of various sensor types has been mounted on the experimental setup. These indirect measurements associated to the hypothesis that all dissipations are related to internal dissipations (i.e. concrete nonlinearities and rebars/concrete sliding) allow for the assessment of the hysteretically dissipated energy. The latter hypothesis is fulfilled by an important design effort on the technological choices for the samples and the boundary conditions as described comprehensively in the Ph.D. thesis of the first author [18] and more concisely in a dedicated paper [19]. A focus is made in this paper on the quasi-static full cyclic loading of one RC beam. This section describes briefly this part of the experimental campaign setup which is necessary to provide the data used in this work.

2

2.2. RC Beams

For the first beam (referenced as HA12-C1B-1), the reinforcement is composed of ten 12mm-diameter reinforcing steel bars in the section of the beam. The standard concrete C25/30 (in the sense of Eurocode 2 [6]) has a 29.7 MPa strength and 28.1 GPa Young's modulus. The reinforcement drawing is given in figures 2a and 2b. For the second beam studied in section 5 (referenced as HA20-C1A-1), the reinforcement is composed of four 20mm-diameter reinforcing steel bars in the section of the beam. The concrete is a standard C25/30 with a 35.0 MPa strength and 26.2 GPa Youngs modulus. The steel reinforcement drawing is given in figures 2c and 2d. More details regarding the geometrical and material characteristics of the beams can be found in [18, 19]. In this study, the global methodology and the identification of the EVDR is developed for the beam HA12-C1B-1. The second beam (HA20-C1A-1) is used in the last part of the paper to validate the methodology and the influence of the degradation state of the structure and the displacement demand on the EVDR.

2.3. Setup

To better understand and visualize the items described in the following sections, a general view of the final experimental setup is presented in figure 3a and schematized in figure 4. Only the quasi-static part of the experimental campaign is considered in this paper. Elastic hinges based upon high performance steel blades are used at both ends to link the beam with the shaking table or the strong floor. The blades have been designed to behave elastically all along the tests. This technical solution avoids by this way the dissipations due to friction or assembly clearance. The weight of the beam is supported by air cushions that considerably reduce the friction forces between the beam and the ground during bending. Indeed, supporting the vertical forces through the beam-end supports would have caused bending cracks due to the 5.9 meters span.

3. Equivalent viscous damping identification procedure

A viscous damping model is a practical — but not entirely satisfactory — way to describe the dissipations occurring in a RC structure to which a dynamic loading is applied. Jacobsen [22] proposed a method to assess an optimal equivalent viscous damping ratio from an energetic point of view. This approach is briefly described below.

3.1. Assessment of the viscous damping ratio for a linear mass-spring-damper system

Let us consider the classical linear mass-spring-damper problem pictured in figure 5, where the different notations used are presented. For an harmonic ground acceleration $\ddot{u}_g(t) = -U_g \cdot \omega^2 \cdot \cos(\omega \cdot t)$, the steady-state displacement and velocity responses are given by equations (2) and (3), where U is the response displacement amplitude, ω is the excitation angular frequency and Φ is the phase angle:

$$u(t) = U \cdot \cos(\omega \cdot t - \Phi) \tag{2}$$

$$\dot{u}(t) = -U \cdot \omega \cdot \sin(\omega \cdot t - \Phi) \tag{3}$$

The energy E_d dissipated by the viscous damper during one displacement half-cycle Γ_u starting at $t = 0$ and ending at $t = \frac{\pi}{\omega}$ is expressed in equation (5) with ω_0 the natural angular frequency of the system:

$$
\begin{aligned}
E_d &= \int_{\Gamma_u} F_D \cdot du \\
&= \int_0^{\frac{\pi}{\omega}} c \cdot \dot{u}(t)^2 dt \\
&= \int_0^{\frac{\pi}{\omega}} c \cdot U^2 \cdot \omega^2 \cdot \sin(\omega \cdot t - \Phi)^2 \cdot dt
\end{aligned}
\tag{4}
$$

Hence:

$$E_d = \frac{\pi}{2} \cdot c \cdot \omega \cdot U^2 \tag{5}$$

For a purely linear spring, the maximum stored elastic energy is reached at displacement U:

$$E_s = \int_0^U k \cdot u \cdot du = \frac{1}{2} \cdot k \cdot U^2 \tag{6}$$

From equations (5) and (6), and provided that $c = 2 \cdot m \cdot \xi \cdot \omega_0$ and $k = m \cdot \omega_0^2$, the viscous damping ratio writes:

$$\xi = \frac{1}{2 \cdot \pi} \cdot \frac{\omega_0}{\omega} \cdot \frac{E_d}{E_s} \tag{7}$$

At this point, it is clear that the viscous damping ratio of a linear oscillator not only depends on the ratio of the dissipated energy during one half-cycle over the maximum stored energy during this same half-cycle, but also on the ratio of the natural angular frequency of the oscillator over the excitation angular frequency.

3.2. Jacobsen's areas method

The expression in equation (7) is exact for the aforementioned ideal case. Jacobsen [22, 23] proposed to extend its use to non-viscous damping. The method was originally used to evaluate the equivalent viscous damping ratio (EVDR) for non-linear frictional system. Since the publication in 1960, many authors have used the here so-called Jacobsen's areas method, with recurrent simplification hypotheses:

- For a linear viscous damper, the dissipated energy over a cycle is linearly proportional to the excitation frequency (see equation (5)). This compensates the inverse function of ω in equation (7) and gives a constant viscous damping ratio ξ. For non-viscous damping, the dissipated energy does not depend on the excitation frequency. Hence, the EVDR actually depends on the excitation angular frequency ω. Except if the excitation frequency is close to the eigenfrequency of the oscillator (i.e. $\omega_0/\omega = 1$), this dependence should be taken into account, otherwise, a significant error on the EVDR is made as illustrated in figure 6.
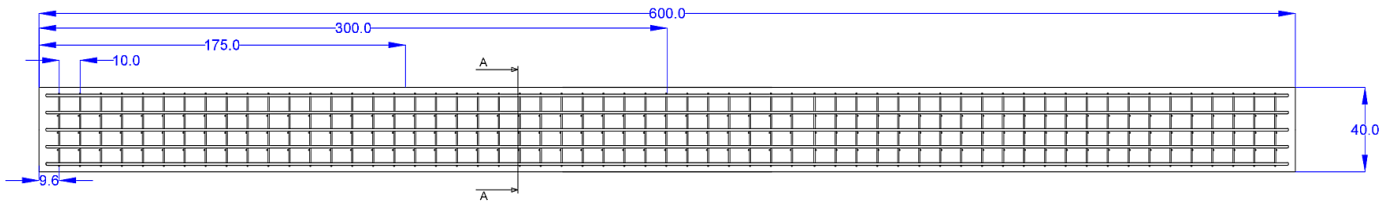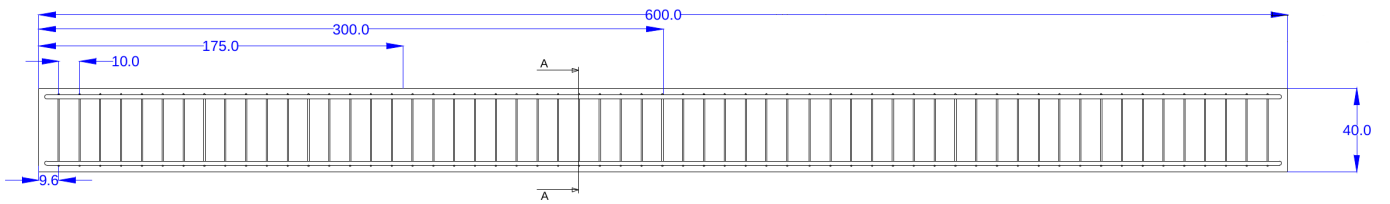
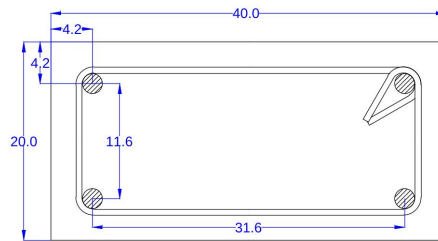(a) Longitudinal reinforcements for HA12-C1B-1 beam
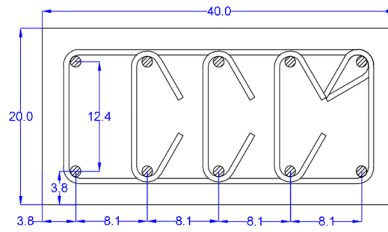
A-A

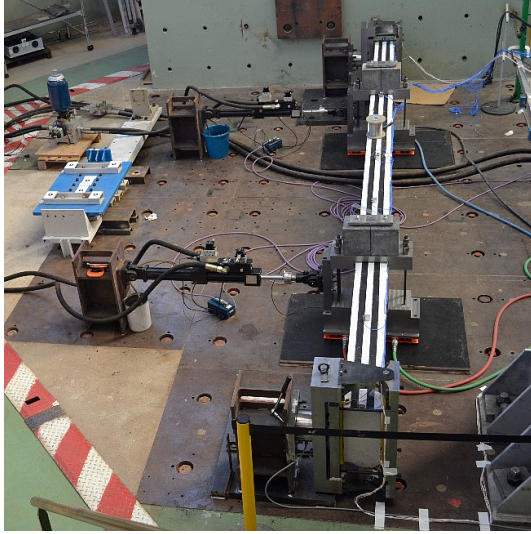(b) Cross-section reinforcements for HA12-C1B-1 beam

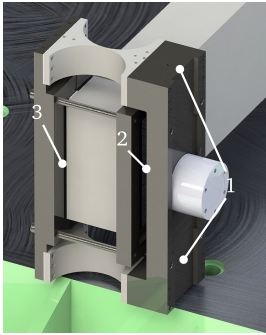(c) Longitudinal reinforcements for HA20-C1A-1 beam

A-A

(d) Cross-section reinforcements for HA20-C1A-1 beam

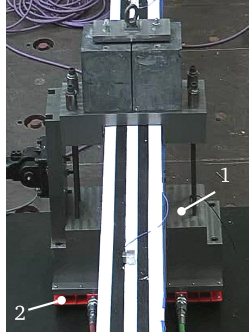Figure 2: RC beams reinforcements (lengths in centimeters)

(a) Overview of the experimental setup

1	Steel blades
2	Clamping frame
3	Load cell

| 1 | Clamping frame |
| 2 | Air cushions |

(b) Focus on beam-end support

(c) Focus on intermediate support

Figure 3: Illustrations of the quasi-static experimental setup on the strong-floor
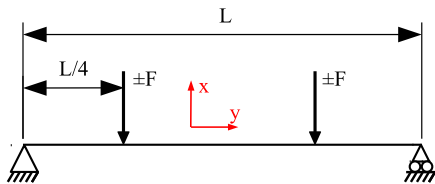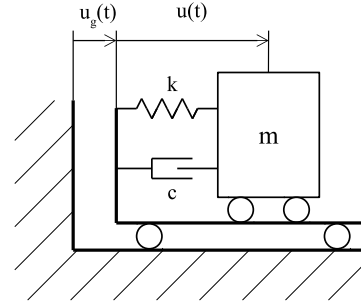

Figure 4: Experimental setup

Figure 5: Notations used for the considered mass-spring-damper oscillating system
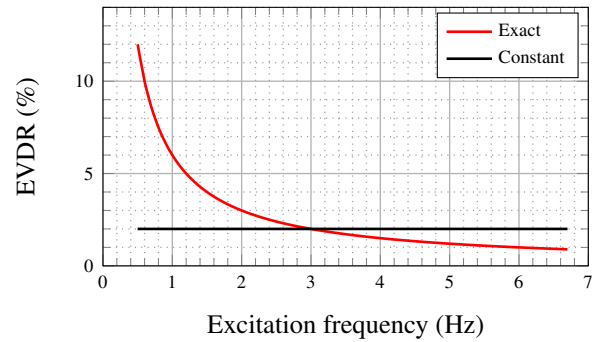

Figure 6: Dependence between EVDR and excitation frequency, example for an EVDR estimated with an excitation frequency of 3 Hz

- In the force-displacement plot in figure 7a, the area enclosed in the half loop equals the dissipated energy E_d. For the sake of simplicity, the maximum stored energy E_s is often evaluated as the area of the right triangle linking the origin and the maximum displacement point. However, in its original publication, Jacobsen [23] rather suggests to use the area under the actual restoring force curve which he calls "skeleton", as depicted in figure 7b to consider nonlinear elasticity.

- When the loops are not symmetric, there is no actual reason to pick up the maximum relative displacement rather than the minimum one when assessing the stored elastic energy. For this reason, Kumar *et al* [27] proposed an approach adapted to asymmetric hysteretic behaviors in soils as depicted in figure 7c. A method inspired from this work and more suitable for nonlinear restoring forces is proposed in figure 7d. The skeleton is computed as the mean force for a given displacement (reached during both loading and unloading). This prevents problems related to softening behaviors.

These observations make the full-cycle skeleton-based method depicted in figure 7d a reasonable choice to assess the EVDR from the full cyclic tests results further exposed. This last method is used after for the computation of the EVDR. Furthermore, the EVDR is identified for the eigenfrequency of the oscillator.
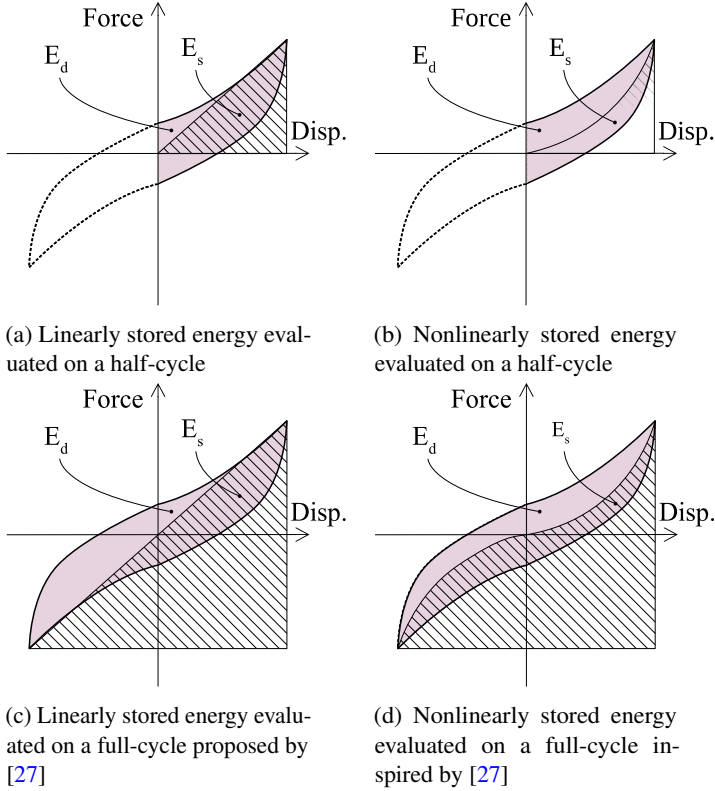
5

(a) Linearly stored energy evaluated on a half-cycle

(b) Nonlinearly stored energy evaluated on a half-cycle

(c) Linearly stored energy evaluated on a full-cycle proposed by [27]

(d) Nonlinearly stored energy evaluated on a full-cycle inspired by [27]

Figure 7: Different ways to apply Jacbosen's areas method [23, 27]

Figure 8: Imposed actuators' displacement and resulting modal displacement of the experimental QSC1 loading

4. Identification of a hysteretic model on experimental data

4.1. Quasi-static full cyclic test

A quasi-static full cyclic loading, labeled QSC1, is carried out thanks to two actuators mounted at positions $\frac{L}{4}$ and $\frac{3 \cdot L}{4}$ with an increasing cycle amplitude. Each cycle of this displacement-driven loading is repeated three times to stabilize the damage state of the beam. The corresponding time-displacement evolution is given in figure 8. To interpret the whole displacement response of the beam as that of a simple degree of freedom oscillator (SDOF), a full-field measurement based upon a commercial digital image correlation method has been used (Videometric [47]). This method provides displacement data throughout the beam, allowing for the projection over the eigenmode shapes [19, 20]. The validation of the assumption of similar displacement fields between 4-point bending test and dynamic loading is exposed in [19]. In the present case, the presented displacement data result from the projection of the displacement field of the beam on the theoretical first mode shape computed thanks to a finite element model of the experimental setup. Thus, they can be considered as an estimation of the first mode displacement: $v(x, t) = q_1(t)\phi_1(x)$, with $q_1(t)$ the first mode displacement and $\phi_1(x)$ the first mode shape. The corresponding force-displacement graph is represented in figure 9.
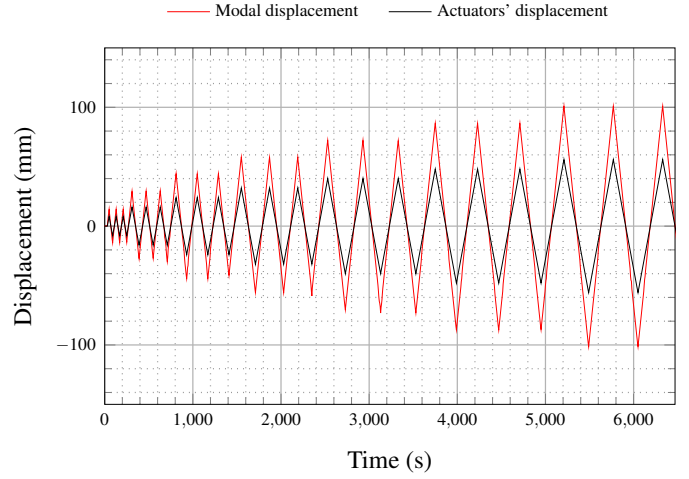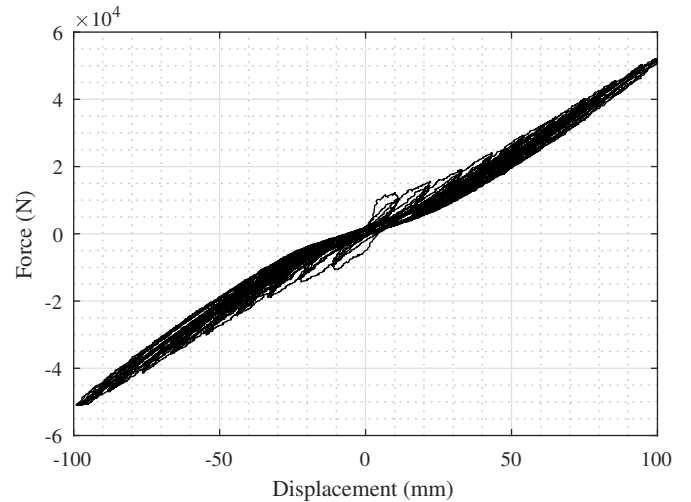

Figure 9: Force-displacement (first mode displacement) measurement for the considered QSC1 test

6

4.2. Formulation of a SDOF hysteretic model for the beam behavior

4.2.1. Objectives

In order to describe the behavior of the beam, a nonlinear oscillator is associated to the first eigenmode. The nonlinear behavior of the first mode has been observed experimentally with a frequency drop from 6.79 Hz to 2.83 Hz (beam HA12-C1B-1) and from 7.16 Hz to 2.97 Hz (beam HA20-C1A-1). This observation is explained by the nonlinear phenomena described and modeled in section 4.2.2. This model is not intended to be general but rather adapted to the QSC1 test (i.e. bending of the beam following the first mode shape). It provides a useful basis for numerical experiments that will be carried out on virtual quasi-static tests in section 5. Moreover, in paper [19], a space-time projection error map is presented, showing no significant error growth during the degradation process. These numerical experiments investigate the uncoupled influence of both the loading amplitude (e.g. displacement, curvature, force, bending moment) and degradation state.

4.2.2. Modeled phenomena

The model presented in this section strongly relies on the work of Moutoussamy [34]. For small displacements applied at the initial state, the beam in bending has a linear elastic behavior, i.e. has a constant stiffness K which can be identified. Beyond a limit displacement δ_d (i.e. displacement at which first crack occurred in concrete) , the beam starts to exhibit nonlinearities. A stiffness decrease is observed during the unloading phase, this indicates the creation and propagation of cracking and motivates the use of the damage mechanics framework [30].

Steel yielding is not observed during the tests and is consequently not taken into account. Nevertheless, hysteresis loops are observed during loading-unloading cycles. It is explained by the existence of friction within the reinforced concrete, e.g. between cracks surfaces or between the steel reinforcements and the surrounding cracked concrete. Hence, a sliding displacement variable u^π is defined [39, 42].

The unilateral effect is taken into account by splitting each internal variable related to damage in two parts. These parts correspond to two independent families of cracks on upper or lower half cross-sections of the beam from either side of the neutral axis depending on the direction of deflection. Supposing a linear behavior of concrete in compression, the beam behavior is mainly driven by the tension area (and the associated damage state). The index i will be used to stand for both direction indexes "+" and "−". A kinematic hardening variable α^π is associated to the friction displacement u^π.

Finally, the last observed phenomenon is the so-called "pinching" effect which consists in a stiffness reduction in the neighborhood of the zero-displacement point that explains the reversed S-shape of the load displacement curve. The origin of this effect is not clearly understood but different hypotheses exist. Several researchers state that this effect indicates a failure driven by shear [3, 36, 2, 35, 11, 48, 1]. However, a shear failure is unlikely to occur with such a flexible beam in four-point bending test. Hence, two explanations are here proposed:
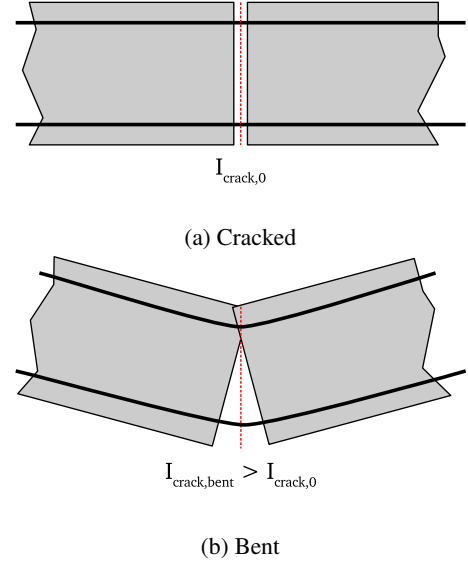

(a) Cracked

(b) Bent

Figure 10: Illustration of the increase of moment of inertia due to crack closure under bending

Mechanism	Observable variable	Internal variable
Displacement	u	
Damage		d_i
Friction		u^π
Kinematic hardening		α^π
Crack closure		η

Table 1: Internal variables of the model

- in the case of a crossing crack, the crack surfaces get into contact when the displacement is high enough (as illustrated in figure 10) thus enlarging the virtual cross section of the beam at the crack location;

- the steel-concrete bond failure induces slipping until the adherence is found again at the interface (inter-locking).

4.2.3. State potential

The thermodynamical framework [30] of the model is defined in this part. Helmoltz's free energy is chosen as state potential, which is a function of the internal and observable variables summarized in table 1:

$$\Psi(u, d_i, u^\pi, \alpha^\pi, \eta) = \Psi^e(u, d_i, \eta) + \Psi^\pi(u^\pi, \alpha^\pi, \eta, d_i) \quad (8)$$

For a linear elastic behavior:

$$\Psi^e = \frac{1}{2} \cdot K \cdot u^2 \quad (9)$$

To take into account the stiffness degradation, the damage variable d_i is introduced:

$$\Psi^e = \frac{1}{2} \cdot K \cdot (1 - d_i) \cdot u^2 \quad (10)$$

The pinching effect only exists along with damage. This is taken into account thanks to a crack closure variable η that evolves
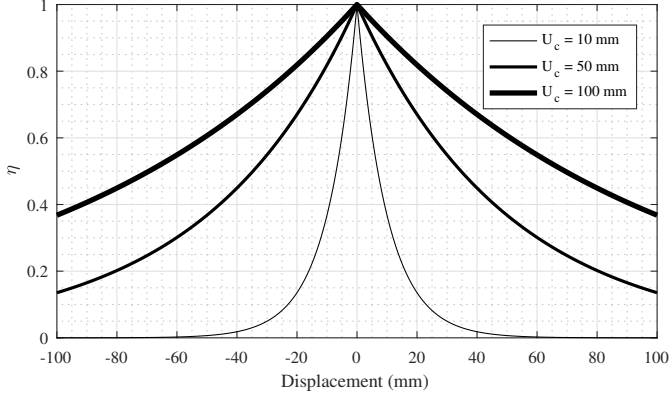
7

Figure 11: Plot of the pinching function over displacement for $d_i = 1$ (0 value corresponds to completely closed cracks)

Par.	Description	Value	Unit
δ_d	Displacement at first crack in concrete	6.4	mm
K_0	Initial stiffness	1.88	N·mm^{-1}
p	Stiffness loss coefficient (=1-d_∞)	0.228	–
q	Fragility coefficient	0.426	–
a^π	Hysteresis loops width	1480	N
b^π	Initial stiffness of the hysteresis loops	74.7	N·mm^{-1}
U_c	Crack closure displacement	54.2	mm

Table 2: Model parameters and identified values

Y_0 is an initial energy threshold:

$$Y_0 = \frac{1}{2} \cdot K \cdot \delta_d^{\ 2} \quad (21)$$

The damage evolution law is chosen similarly to the one of Moutoussamy [34]:

$$d_i = d_\infty \cdot \left(1 - \left(\frac{Y_0}{Y_i^d}\right)^q\right) \quad (22)$$

with $d_\infty \leq 1$ the maximum potential damage (i.e. giving the secant stiffness $K_0 \cdot (1 - d_\infty)$ for an infinite displacement) and q a coefficient driving the slope right after the damage initiation in the force-displacement curve.

For the friction phenomena and the kinematic hardening, the threshold surface is:

$$f^\pi = |F^\pi - X^\pi| \quad (23)$$

However, to take into account hysteresis loops that are nonlinear by nature, a non-associative potential of dissipation is used, as proposed by Armstrong–Frederick [14]:

$$\Phi^\pi = |F^\pi - X^\pi| + \frac{1}{2} \cdot a^\pi \cdot (X^\pi)^2 \quad (24)$$

Then, the flow rules are:

$$\dot{u}^\pi = \dot{\lambda}^\pi \cdot \frac{\partial \Phi^\pi}{\partial F^\pi} = \dot{\lambda}^\pi \cdot \mathrm{sign}(F^\pi - X^\pi) \quad (25)$$

and:

$$\dot{\alpha}^\pi = -\dot{\lambda}^\pi \cdot \frac{\partial \Phi^\pi}{\partial X^\pi} = \dot{\lambda}^\pi \cdot \mathrm{sign}(F^\pi - X^\pi) \quad (26)$$

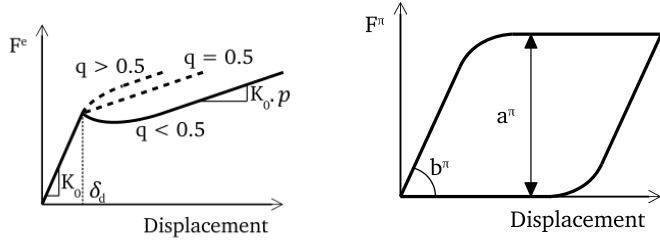$\dot{\lambda}^\pi$ is the plastic multiplier.

4.2.6. Model identification strategy

The model identification is performed thanks to a minimization algorithm applied on the global relative force error ε_F given in equation (27).

$$\varepsilon_F = \sum_{i=1}^{N} \frac{\left(F_i - F_i^{exp}\right)^2}{\left(F_i^{exp}\right)^2} \quad (27)$$

F_i is the total force.

There are 7 parameters to identify, as summarized in table 2. To facilitate the identification process, a sequential procedure is followed:

from 0 (cracks completely closed) to 1 (cracks opened):

$$\eta = d_i \cdot \exp\left(-\left|\frac{u}{U_c}\right|\right) \quad (11)$$

U_c corresponds to the crack closure displacement. Hence, the altered stiffness K_p is defined as follows:

$$K_p(\eta) = K \cdot (1 - \eta) \quad (12)$$

which means that the pinching appears progressively with the damage. Examples of "pinching curves" for a fully damaged beam (i.e. $d_i = 1$) are given in figure 11. Then:

$$\Psi^e = \frac{1}{2} \cdot K_p(\eta) \cdot (1 - d_i) \cdot u^2 \quad (13)$$

If the friction state potential is now considered:

$$\Psi^\pi = \frac{1}{2} \cdot K_p(\eta) \cdot d_i \cdot (u - u^\pi)^2 + \frac{1}{2} \cdot b^\pi \cdot (\alpha^\pi)^2 \quad (14)$$

To summarize, the overall state potential writes:

$$\Psi = \frac{1}{2} \cdot K_p(\eta) \cdot (1 - d_i) \cdot u^2 + \frac{1}{2} \cdot K_p(\eta) \cdot d_i \cdot (u - u^\pi)^2 + \frac{1}{2} \cdot b^\pi \cdot (\alpha^\pi)^2 \quad (15)$$

4.2.4. State laws

The next step is to formulate the state laws by differentiating the state potential in equation (15), namely:

$$F^e = \frac{\partial \Psi}{\partial u} = K_p(\eta) \cdot (1 - d_i) \cdot u + K_p(\eta) \cdot d_i \cdot (u - u^\pi) \quad (16)$$

$$F^\pi = -\frac{\partial \Psi}{\partial u^\pi} = K_p(\eta) \cdot d_i \cdot (u - u^\pi) \quad (17)$$

$$X^\pi = -\frac{\partial \Psi}{\partial \alpha^\pi} = b^\pi \cdot \alpha^\pi \quad (18)$$

$$\quad (19)$$

4.2.5. Flow rules

The energy rate Y_i^d that drives damage is defined by:

$$Y_i^d = \frac{1}{2} \cdot K_p(\eta) \cdot \langle u \rangle_i^{\ 2} \quad (20)$$

8

(a) Parameters influence for a monotonic loading

(b) Parameters influence for a unilateral cyclic loading (without pinching)

Figure 12: Description of some parameters influence on the model behavior

1. the elastic parameter K_0 is identified either on the 1st loading, prior to the 1st nonlinearity (expected at the initial value set for δ_d), or is set arbitrarily to match the 1st measured eigenfrequency, knowing the associated modal mass. If K_0 influences the whole behavior of the beam, its role is difficult to uncouple from the ones of other parameters in the nonlinear domain while it is straightforward in the linear domain;

2. δ_d, p, q are identified on the nonlinear part of the capacity curve (i.e. beyond δ_d) deduced from the test;

3. the last 3 parameters (a^π, b^π, U_c) are identified on the full cyclic QSC1 force time-history.

The effects of the different parameters are graphically described in figures 11 and 12.

4.3. Identification results

The procedure described in section 4.2.6 has been carried out on the different beams tested with QSC1. The results obtained for the beam HA12-C1B-1 are summarized in table 2 and the corresponding error indicator of equation 27 equals $\varepsilon_F = 0.0376$. The behavior of the identified model is illustrated in figure 13a in comparison with QSC1 experimental data. The quality of the identification validates the choices made for the macro-element (RC beam) model. The total force ($F^e + F^\pi$) is plotted in figure 13a.

5. Numerical study of the EVDR dependence on engineering demand parameters

5.1. Engineering demand parameters

The dependence of the EDVR on the degradation and loading levels are investigated. The choice is made in this paper to select the mid-span curvature γ (see figure 14) as the quantity of interest to quantify the loading level. Also, a degradation index Γ is defined as the maximum historic curvature measured at mid-span γ_m over the theoretical first steel yielding curvature γ_y as expressed in equation (31).

The curvature has the advantage over the displacement to be bending-type independent (e.g. 3-point or 4-point bending) since it is defined at the most critical section. Moreover, γ_y can be computed in a predictive way on the basis of design rules

(a) Identified model (overview)
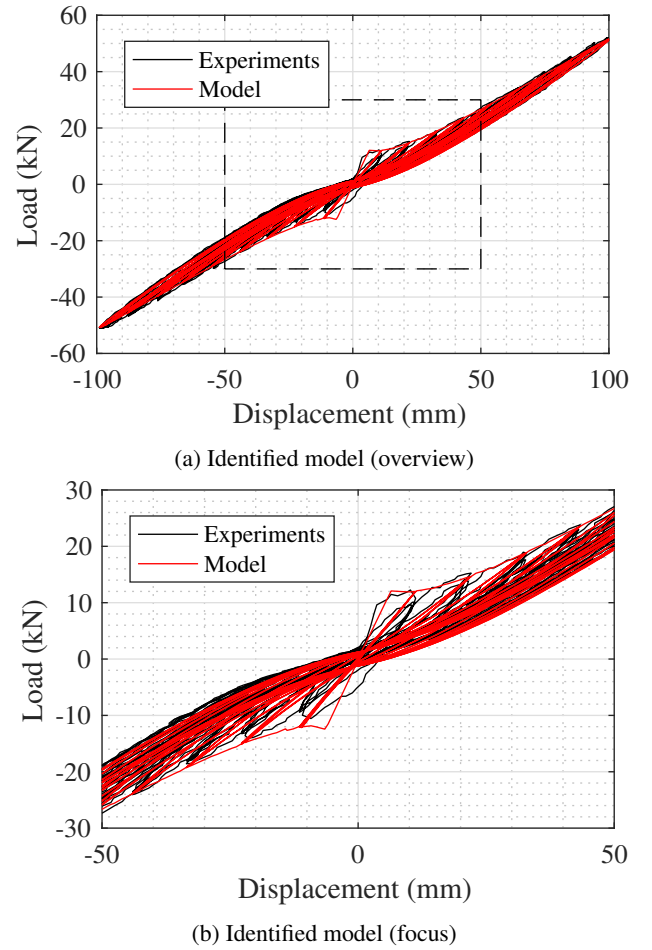

(b) Identified model (focus)

Figure 13: Comparison between model and experiments

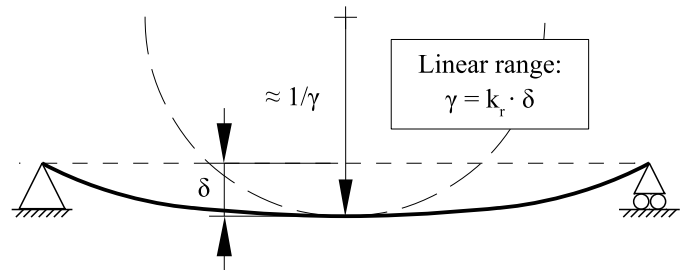Figure 14: Displacement and curvature as engineering demand parameters

9

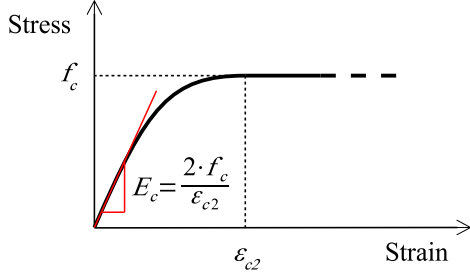Figure 15: Concrete constitutive law from Eurocode 2 [6]

Run	δ_m (cm)	Γ	δ_1 (cm)	δ_2 (cm)	δ_3 (cm)	...	δ_N (cm)
1	0.2	0.018	0.2				
2	0.3	0.027	0.2	0.3			
3	0.4	0.036	0.2	0.3	0.4		
...	...	...	...	...	...	...	
N	10.0	0.91	0.2	0.3	0.4	...	10.0

Table 3: Loading procedure with increasing degradation index – δ_m: maximum displacement; δ_i: amplitude of ith block
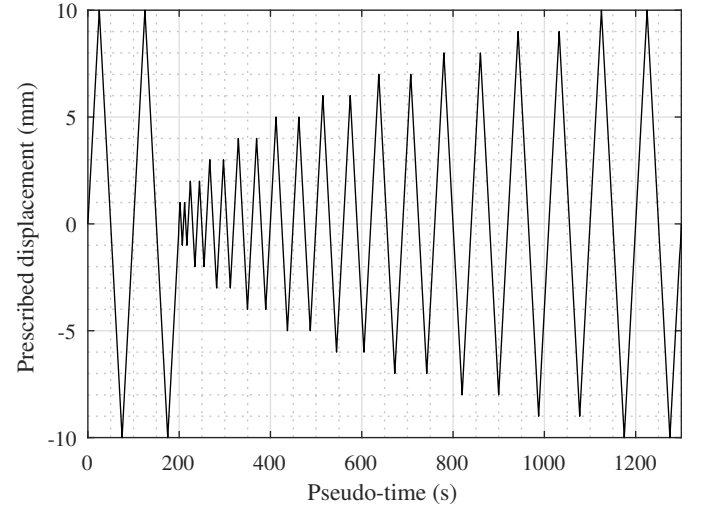

Figure 16: Loading procedure for the sensitivity study (example for $\Gamma = 0.091$)

(such as Eurocode 2 [6]) knowing the material and geometrical properties of the RC section. By using the assumption of non-evolution of the mode shape, one can compute directly by using the analytical mode shape of a dynamically bending beam, the coefficient k_r of the curvature mid-span displacement law in equation (28).

$$\gamma = k_r \cdot \delta \qquad (28)$$

$$\text{with} \quad k_r = \frac{\pi^2}{L^2} \approx 0.28 \text{ m}^{-2} \qquad (29)$$

For the computation of steel-yielding curvature, a Eurocode 2-type constitutive law for the concrete is considered:

$$\sigma_c = \begin{cases} 0 & \varepsilon_c < 0 \\ f_c \cdot \left[1 - \left(1 - \frac{\varepsilon_c}{\varepsilon_{c2}} \right)^2 \right] & 0 \leq \varepsilon_c \leq \varepsilon_{c2} \\ f_c & \varepsilon_{c2} < \varepsilon_c \end{cases} \qquad (30)$$

where ε_{c2} and f_c are the (nonlinear) elastic limits in strain and stress depicted in figure 15. The value of steel-yielding curvature obtained for the studied beam is given in equation (32). It is recalled that the dissipations associated to steel yielding are not in the scope of this study. Hence, Γ is expected to remain within the range [0, 1].

$$\Gamma = \frac{\gamma_m}{\gamma_y} \qquad (31)$$

$$\text{with} \quad \gamma_y = 0.0298 \text{ m}^{-1} \qquad (32)$$

The study of the influence of the degradation level and the loading on the EVDR is challenging for pragmatic reasons. A full cyclic quasi-static test as QSC1 takes about 4 hours to perform (not counting the setup phase). Then, the testing for many degradation states could be very time-consuming. When practical constraints (for example related to the schedule, the cost, or the available equipment) make impossible to investigate experimentally the influence of different parameters on a quantity of interest, numerical experimentation represents an elegant way to address the problem, under the condition that the numerical model used has been validated experimentally. Considering the ability of the model identified in section 4.3 to describe the phenomena taking place during the bending, it can be used as support of virtual quasi-static testing.

5.2. Influence of the degradation and loading levels

5.2.1. Numerical loading

As a side positive consequence for the use of a virtual experimental, there is no spurious dissipation due to external sources. Hence, the validity of the representation of hysteretic dissipation by an equivalent viscous damper is assessed. To study the influence of the degradation level Γ and the prescribed curvature amplitude of the cycle γ, an increasing full cyclic quasi-static displacement loading has been designed and is illustrated in figure 16. Each cycle of displacement amplitude δ is repeated twice so the hysteretic behavior in the 2nd cycle can be considered as stabilized and the energy dissipation due to damage initiation is not taken into account. It is important to note that the first two cycles are equal to the last two in order to remain at the same degradation index Γ of the beam all along the loading.

5.2.2. Observations resulting from the numerical simulations

It is clear from the results given in figures 17a,17b,17c that the degradation index Γ and the displacement amplitude play a major role in the EVDR. Moreover, these two parameters are model-independent. The model includes damage mechanisms, hence, the maximum elastic energy storage decreases with the degradation index Γ (figure 17b). The other important observation is that the energy dissipated does not seem to depend on Γ for the present nonlinear model. However, since the equivalent

10
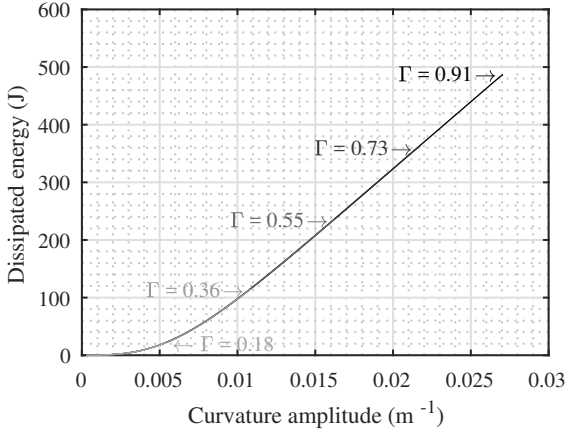
(a) Influence of the cycle amplitude on the dissipated energy E_d per cycle for different degradation indexes Γ
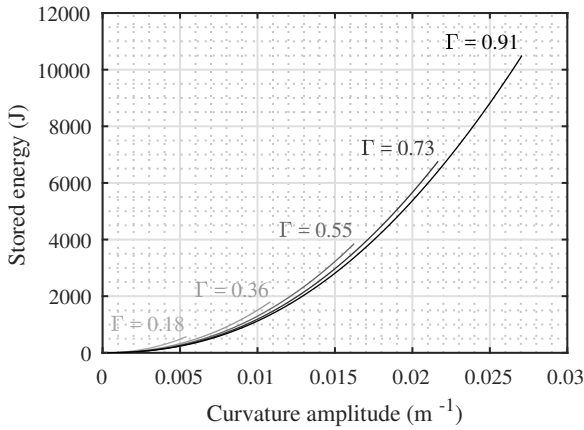
(b) Influence of the cycle amplitude on the stored energy per cycle E_s for different degradation indexes Γ
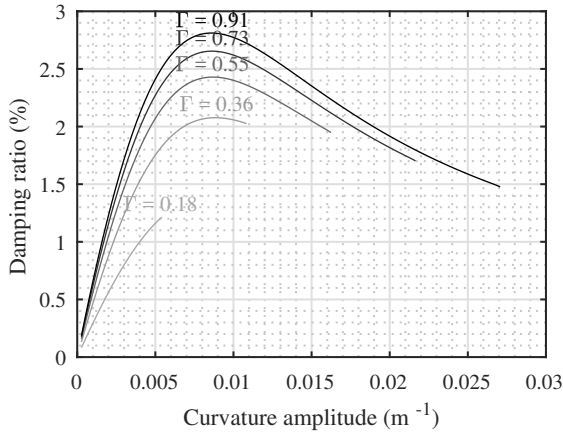
(c) Influence of the cycle amplitude on the equivalent viscous damping ξ_{eq} ratio for different degradation indexes Γ

Figure 17: Influence of the degradation index γ over energies and equivalent viscous damping ratio ξ_{eq} for different cycle amplitudes obtained by Jacobsen's areas method

viscous damping ratio depends on the ratio of the dissipated energy over the stored one, the EVDR seems to increase with respect to the degradation index (see figure 17c).

One can guess a relatively smooth surface fitting the EVDR

points. Then, the highest EVDR point is chosen as the "identification" point of coordinates $(\Gamma_{id}, \gamma_{id}, \xi_{id})$ and is used for the next steps:

- $\gamma = \gamma_{id}$ is fixed at this point, and the best-fitting function $f(\Gamma)$ is identified (thanks to a nonlinear least squares algorithm implemented in the curve fitting toolbox of Matlab) as in figure 18a:

$$f(\Gamma) = \frac{3.679 \cdot \Gamma}{\Gamma + 0.2806} \quad (33)$$

$$\text{then} \quad f(\Gamma) = \begin{cases} 0\ \% & \text{if } \Gamma = 0 \\ 3.679\ \% & \text{if } \Gamma \to +\infty \end{cases} \quad (34)$$

- $\Gamma = \Gamma_{id}$ is fixed at this point, and the best-fitting function $g(\gamma)$ is identified as in figure 18b:

$$g(\gamma) = \frac{0.03759 \cdot \gamma}{\gamma^2 - 0.004994 \cdot \gamma + 8.397 \cdot 10^{-5}} \quad (35)$$

$$\text{then} \quad g(\gamma) = \begin{cases} 0\ \% & \text{if } \gamma = 0 \\ 0\ \% & \text{if } \gamma \to +\infty \end{cases} \quad (36)$$

- the surface given by equation (37) where $\alpha = \frac{1}{\xi_{id}}$ is a normalization coefficient:

$$\xi = \alpha \cdot f(\Gamma) \cdot g(\gamma) \quad (37)$$

The search for an equation of surface in the form of a product of rational functions is motivated by the form of the expression of the EVDR evaluated by Jacobsen's areas method as a ratio between two energies. The degrees of these polynomial functions are deduced from the shape of the curved guessed from the red dots in figures 18a and 18b.

The values obtained for the EVDR depending on both Γ and displacement amplitude γ are represented with the red dots in figure 19a and 19b. In figure 19a, the blue arrow illustrates the loading path actually performed experimentally (curvature amplitude and degradation index increasing together). This is also the loading path used for the identification of the nonlinear oscillator model (figure 8). Each point in the figure 19a (red and black points) corresponds to a different and independent quasi-static numerical computation and not to an extrapolation of the black points. Finally, the black points are, among all the tests performed (red dots), those used to identify the functions $f(\Gamma)$ and $g(\gamma)$ (identification illustrated in figures 18a and 18b).
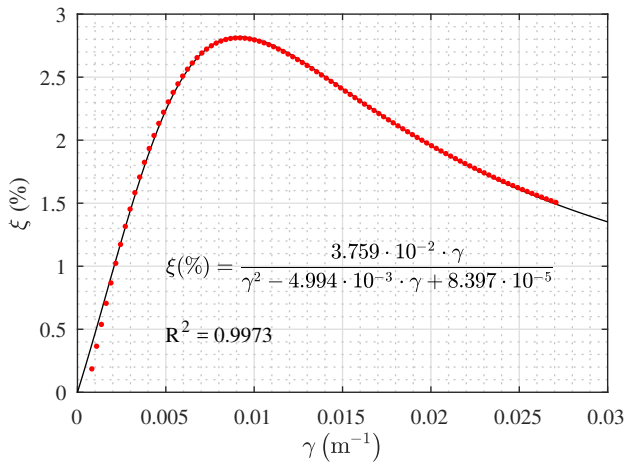
In figure 19b, the surface obtained with the $\xi(\Gamma, \gamma)$ (equation (37)) is compared to the numerical experiments performed (red and black dots). The so-called "damping surface" fits very well the numerical experiments as seen in figure 20. Indeed, only the black dots in figures 19a, 19b have been used for the calibration. The set of red points corresponds to additional numerical experiments considering different loadings for the same beam.

Even though this paper focuses on one particular beam (HA12-C1B-1), several beam designs have been tested as explained in section 2.1. The model proposed in section 4.2 is able to reproduce the behavior of these different designs because the

phenomena involved are the same. The figures 21a and 21b illustrate the fact that similar functions $f(\Gamma)$ and $g(\gamma)$ are obtained for this second tested beam with only a change in the constant values obtained after the identification process exposed in the current section. The parameters identified are different though, and this results in slightly different shapes of the damping surfaces. However, their overall aspects remain the same as shown on figure 22.
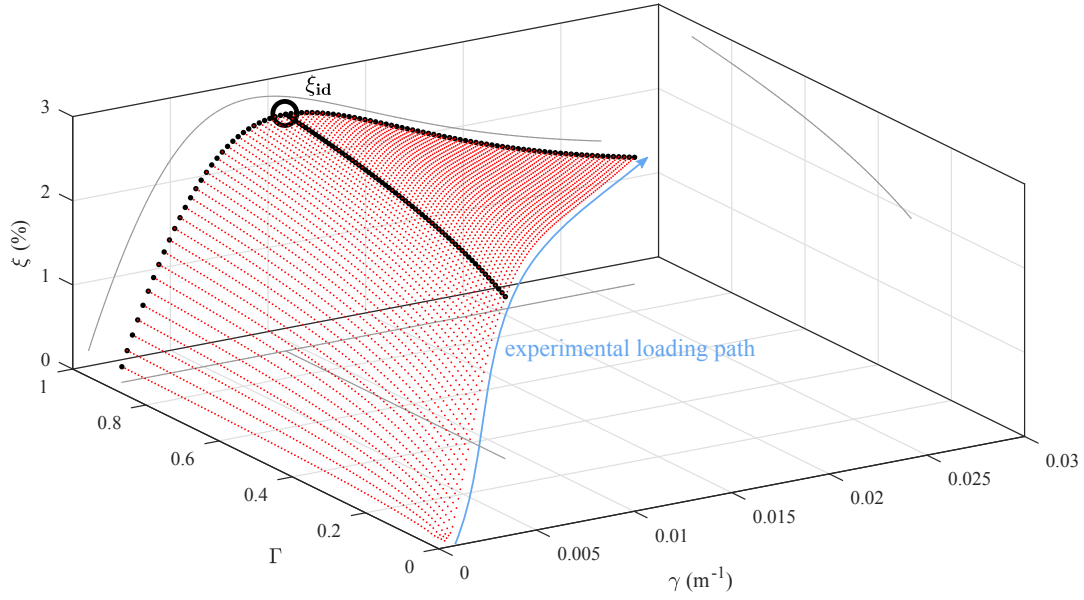

$$\xi(\%) = \frac{3.679 \cdot \Gamma}{\Gamma + 2.806 \cdot 10^{-1}}$$

$$R^2 = 1.0000$$
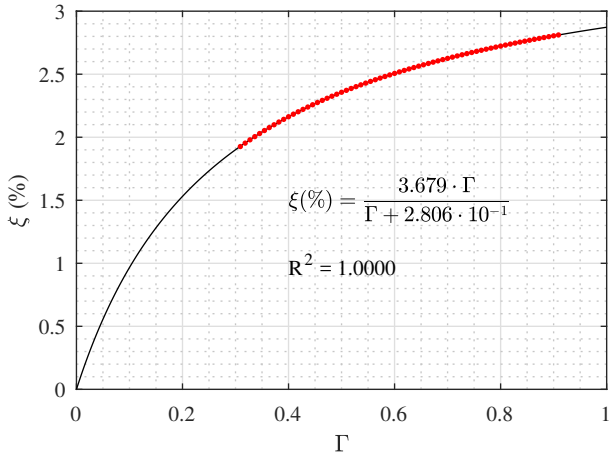
(a) Identified dependence between EVDR and degradation index for a curvature amplitude $\gamma = 0.009204 \text{ m}^{-1}$

$$\xi(\%) = \frac{3.759 \cdot 10^{-2} \cdot \gamma}{\gamma^2 - 4.994 \cdot 10^{-3} \cdot \gamma + 8.397 \cdot 10^{-5}}$$
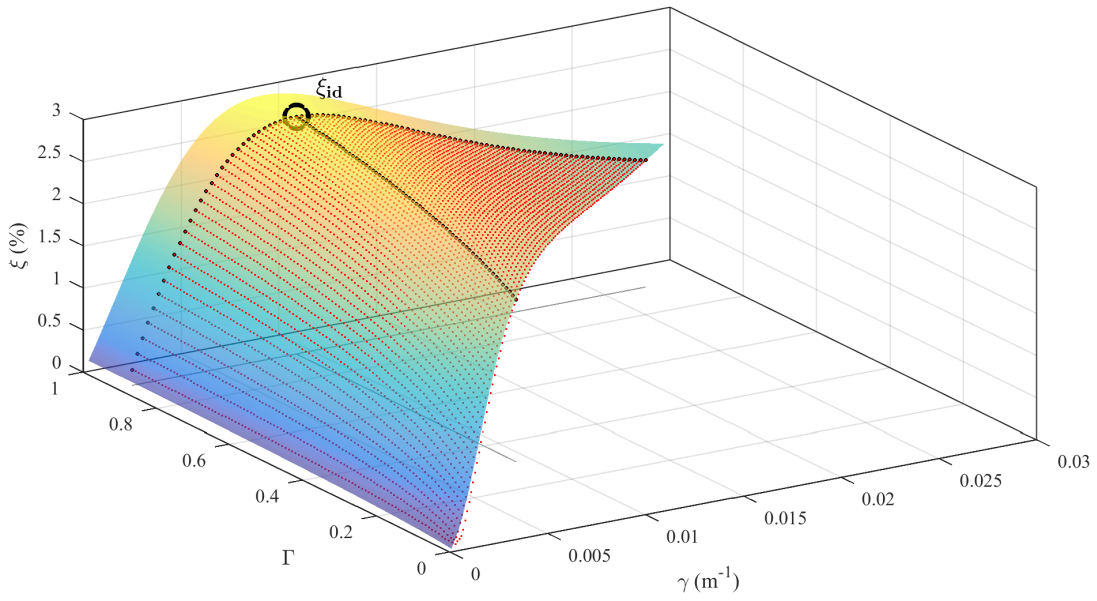
$$R^2 = 0.9973$$

(b) Identified dependence between EVDR and curvature amplitude for a degradation index $\Gamma = 0.73$

Figure 18: Uncoupled identification of dependence between EVDR, degradation index and curvature amplitude

12

(a) EVDR values from numerical simulations

(b) Same as figure 19a with superposed fitted surface

Figure 19: EVDR values for an increasing degradation index Γ and curvature amplitude γ — ξ_{id} represents the identification point for uncoupled functions plotted in figures 18a and 18b; the black dots correspond to the data used for the functions identification of equations 33 and 35

(a) EVDR(%) values from numerical simulations

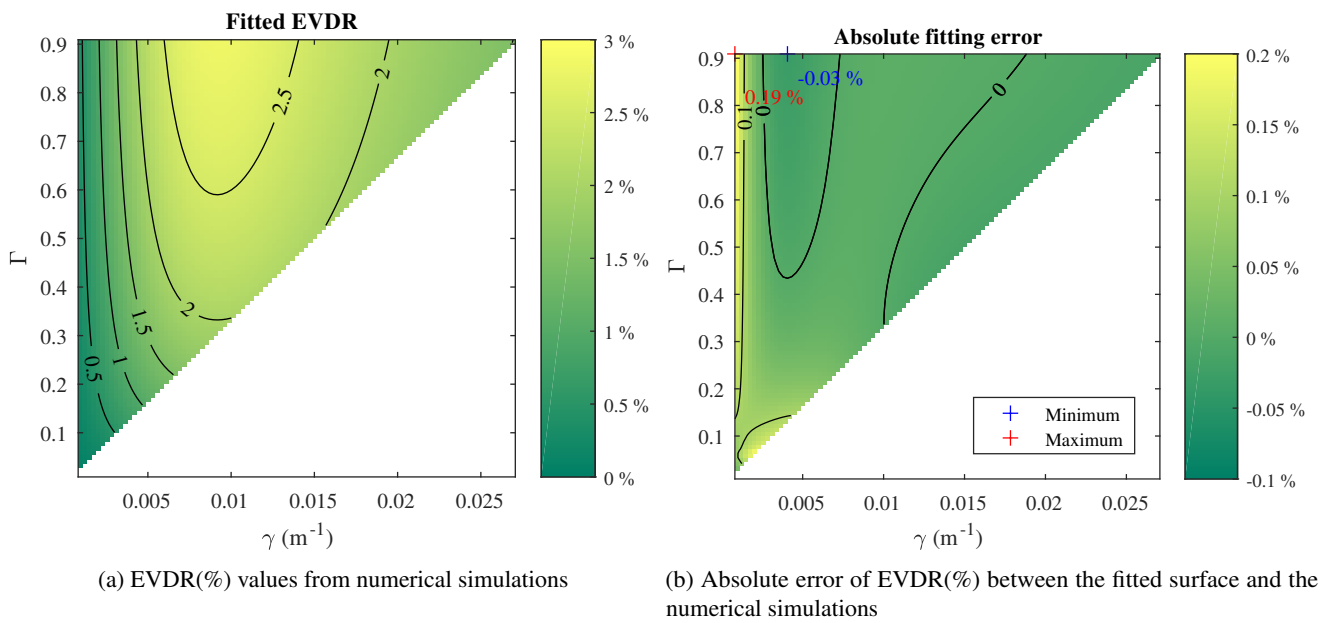(b) Absolute error of EVDR(%) between the fitted surface and the numerical simulations
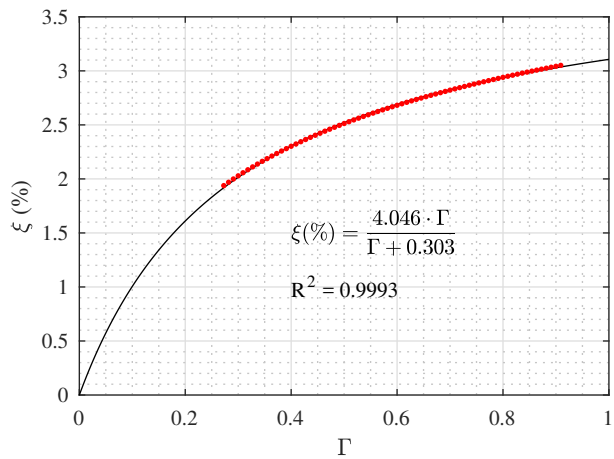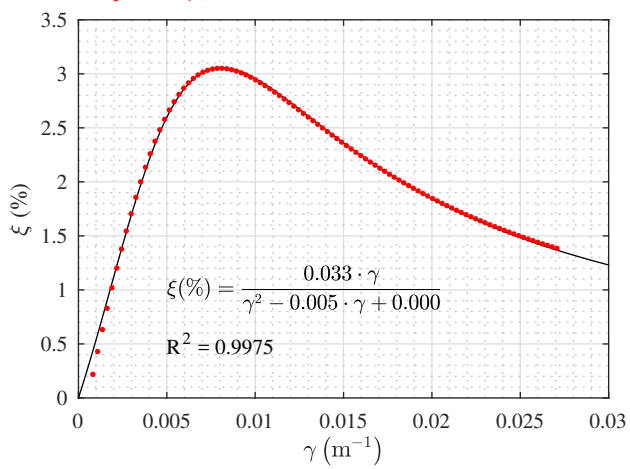
Figure 20: Comparison of the EVDR estimated from the numerical simulations and the corresponding values on the best-fitting surface (interpolated on the identification domain)

(a) Identified dependence between EVDR and degradation index for the curvature amplitude γ_{id}

(b) Identified dependence between EVDR and curvature amplitude for a degradation index Γ_{id}

Figure 21: Uncoupled identification of dependence between EVDR, degradation index and curvature amplitude for beam HA20-C1A-1
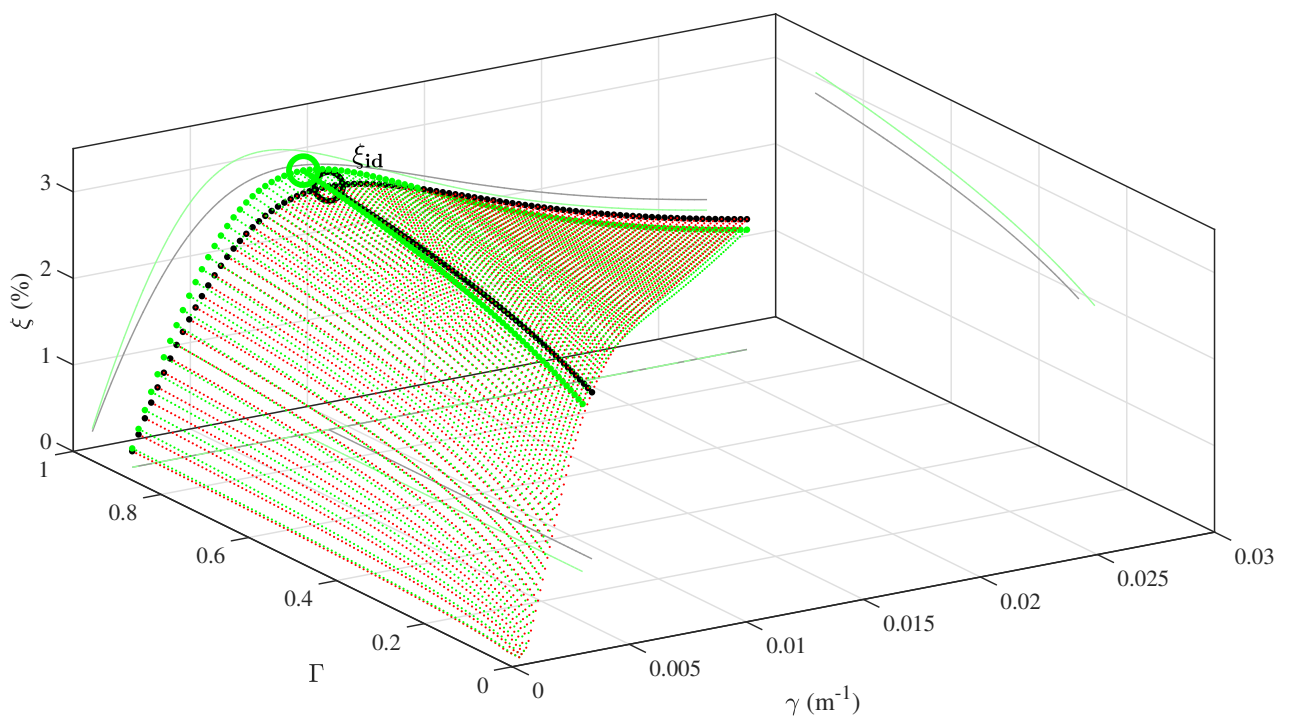
15

Figure 22: Comparison of numerical results for beam HA12-C1B-1 (in red) also drawn on figure 19a and HA20-C1A-1 (in green)

6. Conclusions

In order to improve the relevancy of simplified nonlinear time-history analysis by enhancing the additional viscous damping term, an experimental campaign has been carried out on reinforced concrete beams in both quasi-static and dynamic tests. In particular, a RC beam has been subject to a quasi-static full cyclic four-point bending test. Then, a single-degree-of-freedom model has been proposed and identified to reproduce the experimental restoring force for a prescribed modal displacement measured thanks to a dedicated image correlation based technique. This model has been used to perform additional numerical tests in order to assess both the influence of a degradation index Γ and the amplitude of the curvature at mid-span γ due to the displacement prescribed by the actuators. It is observed that both parameters have a major influence on the equivalent viscous damping. More specifically, the equivalent viscous damping ratio (EVDR) increases with degradation index Γ in an asymptotically way according to the model identified in figure 19b. However, the evolution of the EVDR as a function of the curvature amplitude is not monotonous according to the same model identified in figure 19b: a maximum is reached before the EVDR decreases asymptotically to zero. A function resulting from the product of the two previously identified ones sums-up these observations. It corresponds to the equation of a smooth surface that can be used as a virtual abacus for a more predictive choice of EVDR. It has been shown with two different RC beams (differences regarding concrete and geometry of the reinforcing steel bars) that the evolution of EVDR stays similar according to degradation state of the structure and the displacement demand. Nevertheless, these local quantities (quality of concrete, steel rebars diameter, etc.) affect the coefficients involved in the EVDR surface equation. A perspective of this work is the definition of this link by considering additional experimental and numerical tests.

At this point of this study, it seems important to take into account the variations of EVDR during the nonlinear time-history analysis since this value can evolve from almost 0 % to 3 % for the studied RC beam. For instance, this evolution of the EVDR can lead to a reduction of the local pseudo-acceleration spectrum and as a consequence, of the loading observed by the structure up to 10%. It is worthy noting that the steel yielding is not taken into account in this model, while it is a highly dissipating phenomenon. Many studies focusing on the dissipations related to steel yielding during earthquakes are found in the literature, often proposing an EVDR evolving with respect to the displacement ductility. Hence, the work carried out in this paper is intended to be complementary to these models. The next step of this study will be to use the damping surface as a basis for a fast and physical-wise updating strategy for the EVDR during nonlinear time-history analyses.

Acknowledgments

References

[1] Archundia-Aranda, H. I., Tena-Colunga, A., Grande-Vega, A., 2013. Behavior of reinforced concrete haunched beams subjected to cyclic shear loading. Engineering Structures 49, 27–42.

[2] Bertero, V., Popov, E., jan 1977. Seismic Behavior of Ductile Moment-Resisting Reinforced Concrete Frames. Special Publication 53, 247–292.

[3] Brown, R. H., Jirsa, J. O., may 1971. Reinforced Concrete Beams Under Load Reversals. ACI Journal Proceedings 68 (5), 380–390.

[4] Celik, O. C., Ellingwood, B. R., 2010. Seismic fragilities for non-ductile reinforced concrete frames Role of aleatoric and epistemic uncertainties. Structural Safety 32 (1), 1–12.

[5] Charney, F. A., 2008. Unintended Consequences of Modeling Damping in Structures. Journal of Structural Engineering 134 (4), 581–592.

[6] Comité Européen de Normalisation, 2005. Eurocode 2: Design of concrete structures – Part 1-1: General rules and rules for buildings. Tech. Rep. February 2015, CEN.

[7] Comité Européen de Normalisation, 2005. Eurocode 8 Design of structures for earthquake resistance Part 1: General rules, seismic actions and rules for buildings.

[8] Correia, A. A., Almeida, J. P., Pinho, R., 2013. Seismic energy dissipation in inelastic frames: Understanding state-of-the-practice damping models. Structural Engineering International: Journal of the International Association for Bridge and Structural Engineering (IABSE) 23 (2), 148–158.

[9] Crambuer, R., Richard, B., Ile, N., Ragueneau, F., 2013. Experimental characterization and modeling of energy dissipation in reinforced concrete beams subjected to cyclic loading. Engineering Structures 56, 919–934.

[10] Cruz, C., Miranda, E., 2016. Evaluation of Damping Ratios for the Seismic Analysis of Tall Buildings. Journal of Structural Engineering, 04016144.

[11] D'Ambrisi, A., Filippou, F. C., oct 1999. Modeling of Cyclic Shear Behavior in RC Members. Journal of Structural Engineering 125 (10), 1143–1150.

[12] Elmenshawi, A., Brown, T., jan 2009. Hysteretic energy and damping capacity of flexural elements constructed with different concrete strengths. Engineering Structures 32 (1), 297–305.

[13] Fajfar, P., 2000. A Nonlinear Analysis Method for Performance-Based Seismic Design. Earthquake Spectra 16 (3), 573–592.

[14] Frederick, C. O., Armstrong, P. J., 2007. A mathematical representation of the multiaxial Bauschinger effect. Materials at High Temperatures 24 (1), 1–26.

[15] Frizzarin, M., Feng, M. Q., Franchetti, P., Soyoz, S., Modena, C., 2010. Damage detection based on damping analysis of ambient vibration data. Structural Control and Health Monitoring: The Official Journal of the International Association for Structural Control and Monitoring and of the European Association for the Control of Structures 17 (4), 368–385.

[16] Gulkan, P., Sozen, M. A., 1974. Inelastic responses of reinforced concrete structure to earthquake motions. Journal Proceedings 71 (12), 604–610.

[17] Hall, J. F., 2006. Problems encountered from the use (or misuse) of Rayleigh damping. Earthquake Engineering and Structural Dynamics 35 (5), 525–545.

[18] Heitz, T., 2017. Nonlinear local behaviors and numerical modeling of damping in civil engineering structures in dynamics. Ph.d. thesis, École normale supérieure Paris-Saclay.

[19] Heitz, T., Le Maoult, A., Richard, B., Giry, C., Ragueneau, F., 2018. Dissipations in reinforced concrete components: static and dynamic experimental identification strategy. Engineering Structures (3), 436–451.

[20] Heitz, T., Richard, B., Giry, C., Ragueneau, F., Le Maoult, A., 2017. Damping identification and quantification: experimental evidences and first numerical results. In: 16th World Conference on Earthquake Engineering. Santiago de Chile.

[21] Iwan, W. D., Gates, N. C., 1979. The effective period and damping of a class of hysteretic structures. Earthquake Engineering and Structural Dynamics 7 (3), 199–211.

[22] Jacobsen, L. S., 1930. Steady forced vibration as influenced by damping. Transactions of ASME 52, 169–181.

[23] Jacobsen, L. S., 1960. Damping in composite structures. Proceedings of the 2nd world conference on earthquake engineering 2, 1029–1044.

[24] Jehel, P., 2014. A critical look into Rayleigh damping forces for seismic performance assessment of inelastic structures. Engineering Structures 78, 28–40.

[25] Jehel, P., Léger, P., Ibrahimbegovic, A., 2014. Initial versus tangent stiffness-based Rayleigh damping in inelastic time history seismic analyses. Earthquake Engineering and Structural Dynamics 43, 467–484.

[26] Kowalsky, M. J., 1994. Displacement based design: a methodology for seismic design applied to RC bridge columns. Tech. rep., University of California.

[27] Kumar, S. S., Krishna, M., Dey, A., 2015. Cyclic Response of Sand Using Stress Controlled Cyclic Triaxial Tests. 50th INDIAN GEOTECHNICAL CONFERENCE (December).

[28] Lagaros, N. D., Fragiadakis, M., 2011. Evaluation of ASCE-41, ATC-40 and N2 static pushover methods based on optimally designed buildings. Soil Dynamics and Earthquake Engineering 31 (1), 77–90.

[29] Lee, S. H., Min, K. W., Hwang, J. S., Kim, J., 2004. Evaluation of equivalent damping ratio of a structure with added dampers. Engineering Structures 26 (3), 335–346.

[30] Lemaître, J., 1996. A course on damage mechanics, 2nd Edition. Springer Berlin Heidelberg, Berlin, Heidelberg.

[31] Li, Q. S., Yang, K., Zhang, N., Wong, C. K., Jeary, A. P., 2002. Field measurements of amplitude-dependent damping in a 79-storey tall building and its effects on the structural dynamic responses. The Structural Design of Tall Buildings 11 (2), 129–153.

[32] Liu, K. S., Tsai, Y. B., 2010. Observed natural frequencies, damping ratios, and mode shapes of vibration of a 30-story building excited by a major earthquake and Typhoon. Earthquake Spectra 26 (2), 371–397.

[33] Ministère du développement durable, BRGM, 2018. Plan Séisme: http://www.planseisme.fr/Zonage-sismique-de-la-France.html.

[34] Moutoussamy, L., 2014. Essais hybrides en temps réel sur structures de Génie Civil. Ph.D. thesis, Ecole Normale Supérieure de Cachan.

[35] Otani, S., 1980. Nonlinear dynamic analysis of reinforced concrete building structures. Canadian Journal of Civil Engineering 7, 333–344.

[36] Penzien, J., Celebi, M., 1973. Experimental Investigation into the Seismic Behavior of Critical Regions of Reinforced Concrete Components as Influenced by Moment and Shear. Earthquake Engineering Research Center, Report (73-4).

[37] Priestley, M. J. N., 2003. Myths and fallacies in earthquake engineering, revisited. IUSS press.

[38] Priestley, M. J. N., Calvi, G. M., Kowalsky, M. J., 2007. Displacement-based seismic design of structures. In: NZSEE Conference. Vol. 23. pp. 1453–1460.

[39] Ragueneau, F., 1999. Fonctionnement dynamique des structures en béton - Influence des comportements hystérétiques locaux. Ph.D. thesis, École Normale Supérieure de Cachan.

[40] Ragueneau, F., Mazars, J., La Borderie, C., 1998. Damage model for concrete including residual hysteretic loops: application to seismic and dynamic loading. FraMCos-3, 685–696.

[41] Richard, B., Martinelli, P., Voldoire, F., Chaudat, T., Abouri, S., Bonfils, N., 2016. SMART 2008: Overview, synthesis and lessons learned from the International Benchmark. Engineering Structures 106, 166–178.

[42] Richard, B., Ragueneau, F., 2013. Continuum damage mechanics based model for quasi brittle materials subjected to cyclic loadings: Formulation, numerical implementation and applications. Engineering Fracture Mechanics 98 (1), 383–406.

[43] Richard, B., Voldoire, F., Fontan, M., Mazars, J., Chaudat, T., Abouri, S., Bonfils, N., 2018. SMART 2013: Lessons learned from the international benchmark about the seismic margin assessment of nuclear RC buildings. Engineering Structures 161, 207–222.

[44] Rodrigues, H., Varum, H., Arêde, A., Costa, A., 2011. A comparative analysis of energy dissipation and equivalent viscous dampung of RC columns subjected to uniaxial and biaxial loading. Engineering Structures 35, 149–164.

[45] Rosenblueth, E., Herrera, I., 1964. On a kind of hysteretic damping. Journal of Engineering Mechanics (90), 37–48.

[46] Satake, N., Suda, K.-i., Arakawa, T., Sasaki, A., Tamura, Y., 2003. Damping evaluation using full-scale data of buildings in Japan. Journal of Structural Engineering 129 (4), 470–477.

[47] Videometric, 2018. Videometric: http://www.videometric.com/en/. Tech. rep.

[48] Vintzileou, E., Tassios, T. P., Chronopoulos, M., 2006. Experimental validation of seismic code provisions for RC columns. Engineering Structures 29 (6), 1153–1164.